Reduced Graphene Oxide/Amaranth Extract/AuNPs Composite Hydrogel on Tumor Cells as Integrated Platform for Localized and Multiple Synergistic Therapy

Guanru Chang,[†,‡] Yunlong Wang,[†] Baoyou Gong,[†] Yazhong Xiao,[§] Yan Chen,[§] Shaohua Wang,[†] Shikuo Li,[†] Fangzhi Huang,[†] Yuhua Shen,*[,†,§] and Anjian Xie*[,†]

[†]School of Chemistry and Chemical Engineering, Anhui University, Hefei 230601, People's Republic of China

[‡]School of Chemistry & Chemical Engineering, Huangshan University, Huangshan 245041, People's Republic of China

[§]Collaborative Innovation Center of Modern Bio-Manufacture Anhui University, Hefei 230601, People's Republic of China

(S) **Supporting Information**

ABSTRACT: Integration of multimodal treatment strategies combined with localized therapy to enhance antitumor efficacy and reduce side effects is still a challenge. Herein, a novel composite hydrogel containing rGO, amaranth extract (AE) and gold nanoparticles (AuNPs) was prepared by using AE as both reductant and cross-linking agent. The chlorophyll derivatives in AE were also employed as a photodynamic therapy drug. Meanwhile, AuNPs and rGO both have obvious

photothermal effects and can accelerate the generation of cytotoxic singlet oxygen ($^1O_2$). The temperature increase of rGO/AE/AuNPs precursor is up to 6.3 °C under 808 nm laser irradiation at a power density of 200 mW·cm^{-2}. The hydrogel shell on in situ tumor cells was easily formed and regulated by near-infrared irradiation within 10 min, which could both retain a high concentration of drugs on the lesion site and prevent them from migrating to normal tissue, thus reducing the side effects. Compared with rGO/AE and AE, rGO/AE/AuNPs showed a remarkably improved and synergistic antitumor effect. The hydrogel possesses good biocompatibility and high hydrophilicity and could be used for loading chemotherapeutics, which provides a new approach for located and multiple antitumor therapies.

KEYWORDS: reduced graphene oxide, amaranth extract, gold nanoparticles, composite hydrogel, multiple antitumor
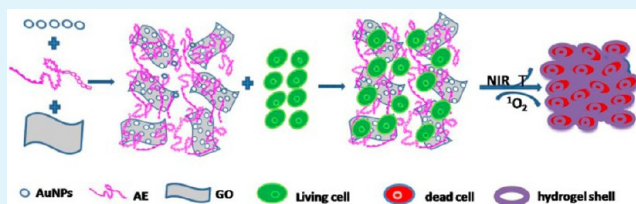
INTRODUCTION

Cancer is one of the most common causes of death worldwide and remains a serious threat to human health. Among anticancer treatments,[1] photothermal and photodynamic therapies have increasingly attracted much attention for their many advantages, such as low cost, highly localized and specific tumor treatment, enhanced therapeutic efficacy, reduced side effects, and minimal trauma to tissues.[2,3] For photodynamic therapy drugs (PDTs), the selective uptake of a photosensitizer (PS) by tumor tissue can produce reactive oxygen species (ROS) under NIR irradiation, then results in apoptosis or necrosis. The implementationphotothermal therapy (PTT) relies on the development of photothermal agents generating heat from light absorption.

Recently, a wide range of inorganic nanomaterials with strong optical absorption in the NIR region, such as quantum dots,[4] gold nanoparticles (AuNPs),[5,6] and upconversion nanoparticles[7] have been used as photothermal agents for PTT treatment. AuNP-assisted photothermal treatment can be targeted with heat in each individual cell of a lesion, thereby improving the controllability of hyperthermia and the selective killing of tumor cells.[8] The green synthesis of AuNPs with high efficiency in absorbing NIR radiation using lemongrass extracts

as reductant has been reported.[9] In addition, some natural photoactive pigments, such as chlorophyll,[8,10] carotenoid,[11] riboflavin,[12] and hypocrellin[13] have been intensively investigated due to their remarkable curative effects in PDT and for the development of new types of PS. Epidemiological studies showed that a high intake of vegetables is correlated with a low incidence of cancer and cardiovascular disease. And ascorbic acid and natural photoactive pigments are found in high concentrations in vegetables and suggested to be involved in the protection against the diseases.[14] Therefore, it is meaningful that amaranth extracts (AEs) are employed as a natural multifunctional platform and an interesting alternative to photoactive pigments.

Graphene and its functionalized derivatives have attracted much attention all over the world and have been well used as an important building block for the self-assembly of supramolecular hydrogels with integrated functionalities and the advantage in many application fields.[15−18] More important, graphene oxide (GO) possesses unique features such as high

Scheme 1. Illustration of the Formation Process and the Antitumor Mechanism of the Composite Hydrogel Shell
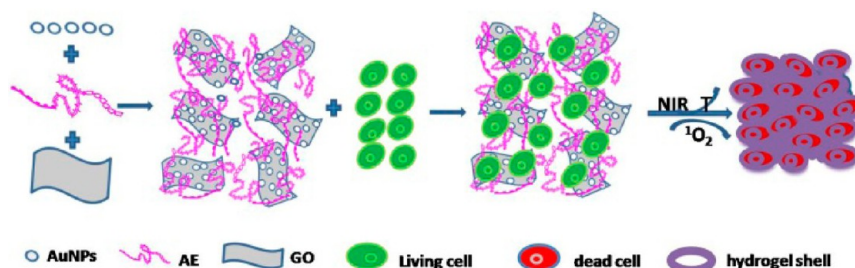
dispersibility in water and physiological environments, good biocompatibility, and convenient chemical modification,[19] which are highly propitious to biological applications. Due to its excellent photon-thermal transfer efficiency under NIR irradiation, reduced graphene oxide (rGO) has also been used for PTT in vitro[20,21] and in vivo[22] for combined PTT and chemotherapy or PDT.[23] Although researchers have made great efforts to combine PS with graphene or gold nanostructures for PDT/PTT, limitations, such as, complicated synthetic process, poor PS loading efficiency and prolonged skin photosensitivity arising from low localized accumulation of PS still exist.[24−27] To overcome the aforementioned drawbacks, it is of great importance to establish PDT/PTT integrated systems with high surface area, versatile surface modification and avid cell uptake.[28]

Toward this goal, herein, we fabricated a highly integrated multifunctional hydrogel system that contained rGO, AE and AuNPs for high-performance antitumor therapy. To our knowledge, the direct use of AE as a low toxicity and eco-friendly PS for antitumor, a cross-linking agent for the formation of rGO-based hydrogel and a green reductant for the preparation of AuNPs has not been reported. Especially, this composite hydrogel, the combination of PTT and PDT as well as localized gelation on tumor cells controlled by NIR irradiation for the maximum therapeutic efficacy with minimal side effects, also has not been mentioned. This hydrogel has characteristics of simple preparation process, low cost and good biocompatibility. As illustrated in Scheme 1, after cells are cultured with the precursor solution of rGO/AE/AuNPs and subjected to laser irradiation, a hydrogel shell on cells in situ was easily formed which can both improve the enrichment degree of PS and photothermal agents around tumor cells, and prevent them from spreading to normal tissue. Meantime, the tumor cells are killed by the $^1O_2$ released from AE and oxygen as well as by the local increase in temperature. The composite hydrogel shows remarkable improved and synergistic antitumor effects, and may be a potentially new tool for cancer treatment through sequential irradiation.

EXPERIMENTAL SECTION

Materials and Characterization. Fresh amaranth leaves were purchased from a local market (Hefei, Anhui, P. R. China). Graphite powder was from Huatai Lubricant Sealing S&T Co., Ltd. (Qingdao, Shandong, P. R. China). FITC-dextran (M_w 70 kDa), dimethyl sulfoxide (DMSO), 2,2,6,6-Tetramethylpiperidine (TEMP), n-dodec-yl-β-D-maltoside (β-DM), trimethylglycine (Tricine) were obtained from Aladdin Reagent Database Inc. (Shanghai, P. R. China). Fetal calf serum (GIBCO), Dulbecco's Modified Eagle Medium (DMEM), pancreatin (0.25% EDTA, GIBCO), double resistant, 3-(4,5-dimethyl-2-thiazolyl)-2-5-diphenyl-2H-tetrazolium bromide (MTT), Hoechst 33342 and propidium iodide (PI) were from Sangon Company (Shanghai, P. R. China). 1,3-Diphenylisobenzofuran (DPBF) was

purchased from Acros Organics. Concentrated sulfuric acid (H_2SO_4), hydrochloric acid (HCl), potassium permanganate ($KMnO_4$), sodium nitrate ($NaNO_3$), hydrogen peroxide (H_2O_2), chloroauric acid ($HAuCl_4$) were purchased from Chemical Shanghai Reagent Co. All chemical reagents were of analytical grade and used without further purification.

FTIR spectra were recorded using a NEXUS-870 spectropho-tometer (Thermo Fisher, Waltham, MA; frequency range, 4000−500 cm^{-1}) with the KBr pellet method. X-ray diffraction (XRD) was conducted using a DX-2700 X-ray diffractometer in the range of 8−80° with a step size of 0.02°. Raman spectroscopy was performed on an inVia-Reflex Raman Microscope equipped with a 532 nm laser. X-ray photoelectron spectroscopy (XPS) was performed on an ESCALAB-MKII spectrometer (VG Co., U.K.) with Al Kr X-ray radiation. Scanning elecrton microscopy (SEM) images were obtained on a S4800 ESEM FEG scanning electron microscope. Transmission electron microscopy (TEM) images were obtained using a JEM 2100 instrument. ESR spectroscopy was carried out on a BRUKER E500 spectrometer. Atomic force microscopy (AFM) images were performed by a Veeco DI scanning probe microscopy MultiMode VIII at a scan rate of 2 Hz. The static contact angle of the hydrogel film was measured using a DSA10-Mk2 contact angle goniometer (Kruss, German) at 25 °C. UV−vis−NIR absorption spectra of the samples were recorded using a UV-3900 spectrophotometer (Hitachi, Japan) over the range of 200−1000 nm. IR thermal imaging was performed with an IR thermal camera (Fluke, Everett, WA). Photoluminescence spectra were measured with a FL spectropho-tometer (F-4500, Hitachi, Japan). The optical density (OD) values of the MTT assay were obtained using a RT-2100C spectrophotometric microplate reader (Rayto, Shenzhen, P. R. China). Fluorescence images were recorded using a DMI3000B inverted fluorescence microscope (Leica, Germany).

Preparation of rGO/AuNPs/AE Hydrogel. GO was synthesized from graphite by modified Hummers method.[29] Fresh amaranth leaves were cleaned and dried at room temperature, then were mixed with anhydrous ethanol, quartz sand and $CaCO_3$ powder. The mixture was ground using a mortar and pestle and then filtered. The AE was obtained by drying under vacuum at low temperature and reserved for further use.

AuNPs were prepared by mixing aqueous $HAuCl_4$ solution (10.0 mL, 10^{-3} M) and AE solution (5.0 mL, 6 mg·mL^{-1}) in a glass vial. Then, the mixture was stirred gently for 1 min and then left undistured for at least 12 h when reduction of $AuCl_4^-$ in the reaction mixture was completed. The obtained AuNPs were centrifuged (8000 rpm × 6 min) and washed with deionized water three times before further use. Then, 3 mg of the obtained AuNPs was added into GO (8 mL, 2.0 mg·mL^{-1}) and AE solution (2 mL, 10 mg·mL^{-1}) to get a homogeneous solution named rGO/AE/AuNPs precursor. The precursor was placed into a glass vial, which was followed by laser irradiation (660 nm, 200 mW·cm^{-2}) for 10 min to form the composite hydrogel. The distance between the precursor and the light source was maintained at 10 cm.

In a control experiment, aqueous solutions of GO (4 mL, 4 mg·mL^{-1}) and AE (1 mL, 20 mg·mL^{-1}) were prepared and then mixed directly to get rGO/AE hydrogel at room temperature.

Measurement of Singlet Oxygen Generation. The generation of singlet oxygen was determined by monitoring the decrease of the
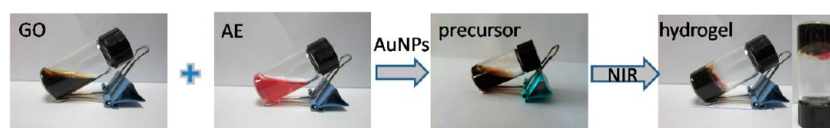
Figure 1. Digital photos of GO, AE and precursor as well as the formation process of rGO/AE/AuNPs hydrogel.
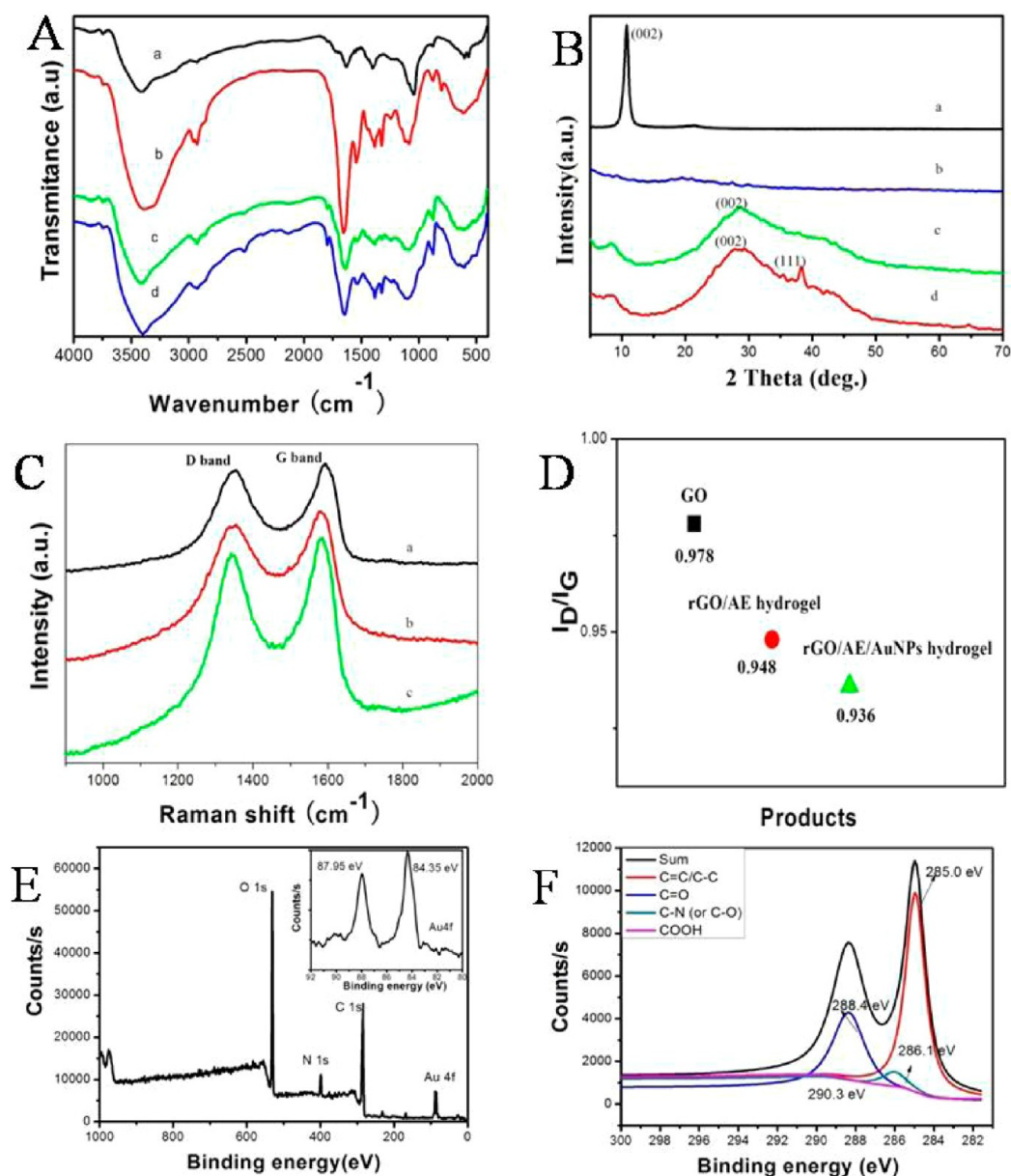

Figure 2. (A) FTIR spectra and (B) XRD patterns of (a) GO, (b) AE, (c) rGO/AE hydrogel, and (d) rGO/AE/AuNPs hydrogel; (C) Raman spectra of (a) GO, (b) rGO/AE hydrogel, and (c) rGO/AE/AuNPs hydrogel; (D) I_D/I_G values in Raman spectra of GO, rGO/AE hydrogel and rGO/AE/AuNPs hydrogel; (E) XPS survey and (F) C 1s core level spectra of rGO/AE/AuNPs hydrogel, respectively. (E, inset) Au 4f XPS spectrum of the hydrogel.

absorption at 410 nm from the decomposition of DPBF.[30] Briefly, 20 mL of DPBF (1.75 mmol) was mixed with 1 mL of precursor. Then, the mixture was irradiated with a 660 nm laser source at 200 mW, and its absorption spectra were recorded at predefined time (ranging from 0 to 20 s) on a UV-3900 spectrophotometer. The experiment was independently repeated at least three times.

In a typical experiment, AE (2.0 mg), TEMP (248.6 mg) and β-DM (5.3 mg) were mixed with Tricine-NaOH buffer solution (50 mL, 50 mmol·L^{-1}, pH 8.0) to prepare sample. After being saturated with oxygen, the sample (80 μL) was sealed in a glass capillary and

illuminated for 20 min with 660 nm red light. electron spin resonance (ESR) spectroscopy of sample was carried out on a BRUKER E500 spectrometer with the followings parameter settings: microwave power and frequency, 0.998 mW and 9073 MHz; modulation amplitude and frequency, 1 G and 100 kHz; sweep time, 60 s.

Cytotoxicity Assay and Uptake Study. For comparative studies, the concentration of GO and AE are 2.0 mg·mL^{-1} and 10 mg·mL^{-1}, and the volume ratio of GO to AE is 4:1 in MTT assay. The precursor solution of AE, rGO/AE, and rGO/AE/AuNPs, respectively, were filtered to remove contaminants and pathogenic bacteria with a PVDF
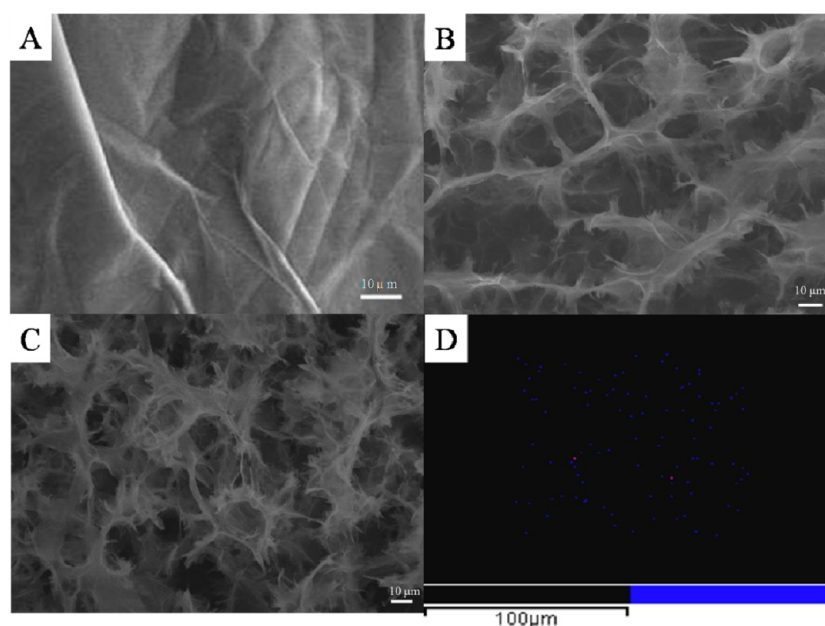
Figure 3. SEM images of (A) GO, (B) rGO/AE hydrogel and (C) rGO/AE/AuNPs hydrogel; and (D) element distribution of Au in rGO/AE/AuNPs hydrogel.

syringe filter, and were subsequently diluted by DMEM with the volume ratio of precursor to medium ranging from 1 to 0.001. HeLa cells or Chinese hamster ovary cells (CHO cells) were seeded (5 × 10³/well) into 96-well plates and incubated for 24 h (37 °C, 5% CO₂). After removing the culture medium, 100 μL of fresh culture medium that contained different concentrations of the precursor was added to each well. The phototoxicities of the precursors were investigated by 660 nm irradiation for 10 min. Following incubation for 24 h, the culture medium was replaced with 20 μL of MTT solution (5 mg·mL⁻¹) and further cultured for 4 h. Then, 150 μL of DMSO was added to dissolve formazan crystals, which were formed during the reductive cleavage of MTT by mitochondrial succinate dehydrogenases of living cells. The absorbance of formazan crystals at 490 nm was measured using a spectrophotometric microplate reader. Culture medium and cells only treated with culture medium were served as a blank group and a negative control group, respectively. The measured OD values of the blank, control and experimental groups were coded as OD_{bla}, OD_{con}, and OD_{exp}. Cellular survival rates were calculated by using the following equation.[31]

$$\text{survival rate (\%)} = \frac{OD_{exp} - OD_{bla}}{OD_{con} - OD_{bla}} \times 100$$

Fluorescence Image. For fluorescence microscope imaging, HeLa cells were seeded (5 × 10⁴/well) in 6-well plates and incubated for 24 h (37 °C, 5% CO₂). Afterward, 3 mL of fresh DMEM medium containing 1 mL of rGO/AE or rGO/AE/AuNPs precursor were added into each well. After being incubated for 6 h, the plate was exposed to 660 nm laser light for 10 min. Then, the HeLa cells were stained with 0.5 mL of Hoechst 33342 (1 μg·mL⁻¹) or 0.5 mL of PI (1 μg·mL⁻¹) for 20 min in the darkness. Dual fluorescence-stained cells were washed with PBS and observed under an inverted fluorescence microscope. All experiments were carried out in triplicate.

To study the cellular uptake of dextran,[32] HeLa cells (5 × 10⁴/well) were seeded in 6-well plates and cultured in medium for 24 h (37 °C, 5% CO₂). After complete adhesion, the cells were washed twice with serum-free medium, and incubated with fresh serum-free medium that contained FITC-dextran (1 mg·mL⁻¹) and the rGO/AE/AuNPs precursor for 1 h. Then the cells were washed with PBS buffer to remove the excess precursor and FITC-dextran, and observed under a fluorescence microscope with a 488 nm laser.

■ RESULTS AND DISCUSSION

Formation and Characterization of rGO/AE/AuNPs Hydrogel. It was reported that concentration of GO lower than 1.0 mg·mL⁻¹ caused difficulty in gelation, whereas concentration higher than 6.0 mg·mL⁻¹ came across problem with dispersing uniformly in the aqueous solution.[33] Considering good biocompatibility and low toxicity, the composite hydrogel with high water content and appropriate gelatin speed would be favorable for application in localized peritumoral injection or clinical therapy. As shown in Figure 1, both AE and GO are homogeneous solution. The precursor only became viscous and no hydrogel was formed at mild environment without NIR irradiation. However, through sequential NIR irradiation, the precursor changed into the semisolid composite hydrogel. These results demonstrate that NIR irradiation is conducive to initiating and accelerating the formation of the composite hydrogel. The formation of rGO/AE/AuNPs hydrogel can be ascribed to multiple interactions in the precursors solution: (1) the reduction of GO to rGO caused by excess AE was confirmed by subsequent FTIR, XRD, and Raman measurements; (2) due to excellent photothermal effects of rGO and AuNPs, the temperature increase of precursor under NIR irradiation, weakens the intermolecular hydrogen bonds between water molecules and rGO, and results in the formation of dewatered rGO sheets; (3) the π−π stacking and hydrophobic interaction among rGO sheets are further enhanced,[34] together with electrostatic attraction between positively charged AuNPs and negatively charged GO sheets, then the hydrogel is formed.

The FTIR spectrum of the GO in Figure 2A (a) reveals the presence of −OH (3400 cm⁻¹), C=O (1728 cm⁻¹), C=C (1621 cm⁻¹) and C−O−C (1050 cm⁻¹) stretching of epoxy groups. The three characteristic absorbance peaks of AE at 1657, 1546, and 1240 cm⁻¹ in Figure 2A (b) are assigned to the C−O stretching vibration of −NHCO− (amide I), the N−H bending vibration of −NH₂ (amide II), and the C−N bending vibration of −NHCO− (amide III).[30] The band at 1078, 1400 cm⁻¹ could be attributed to the presence of C−OH and C−O−
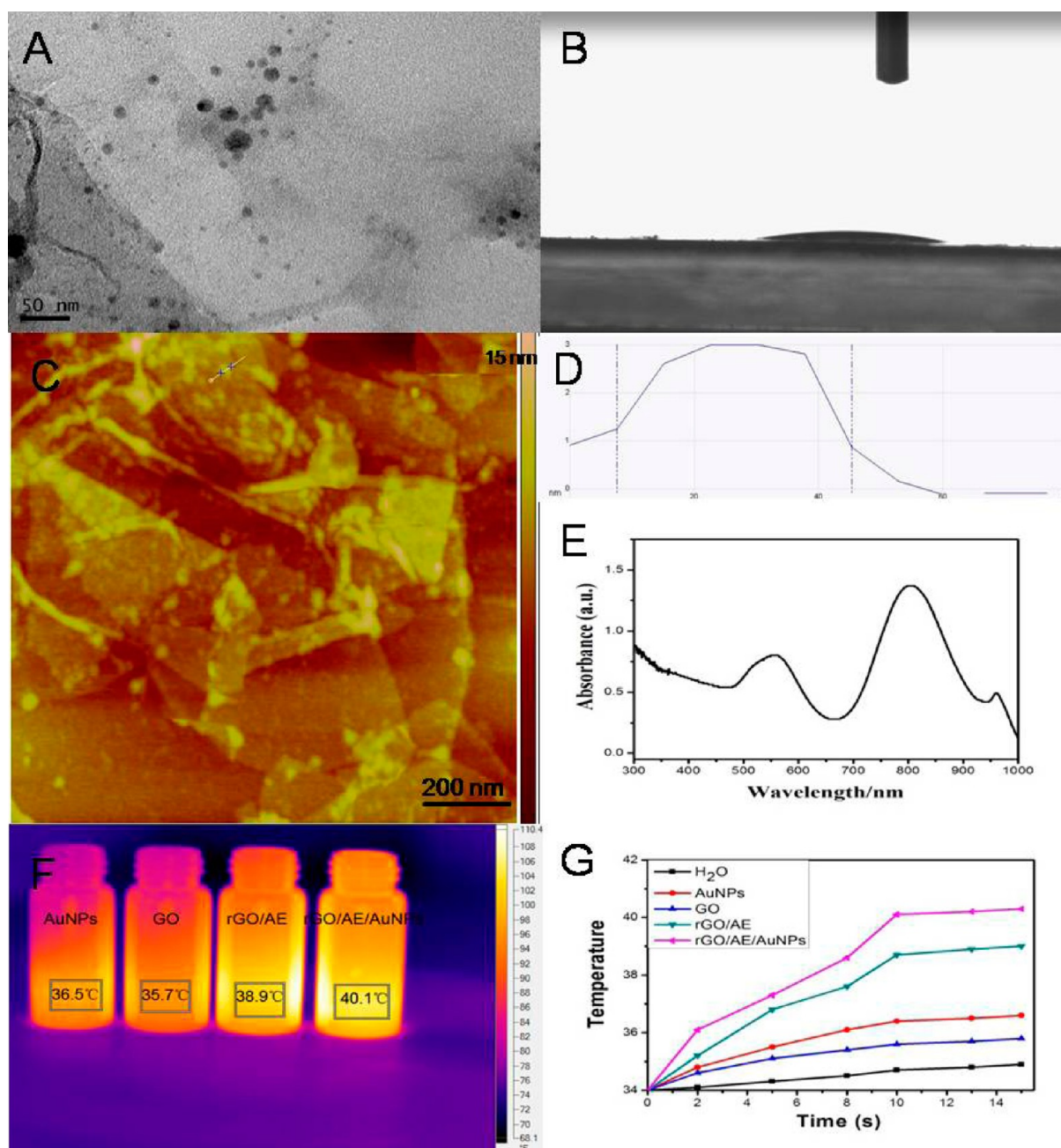
Figure 4. (A) TEM image, (B) static contact angle, and (C) AFM image of rGO/AE/AuNPs hydrogel; (D) cross-sectional analysis of AuNPs attached onto the surface of rGO sheets; (E) UV−vis−NIR absorption spectrum of AuNPs prepared by the green reduction process using AE; (F) IR thermal images of samples under NIR irradiation for 10 min; and (G) temperature variation of samples at different time intervals when exposed to the NIR laser.

C groups of reducibility polysaccharides and polypeptide amino acid.[35] Figure 2A (c) shows the FTIR spectrum of the obtained rGO/AE composite hydrogel, which indicates the disappearance of −COOH (1728 cm^{-1}) and epoxy groups (1050 cm^{-1}) of GO, and the appearance of a strong absorbance peak at 1656 cm^{-1} associated with the amide bonds. Meanwhile, the N−H bending vibration of AE has shifted from 1540 to 1546 cm^{-1} and the peak intensity of the acetylated amino group −NHCO−(amide II and amide III) has decreased. These results disclose that the epoxy and alkoxy groups on the surfaces of GO were gradually removed by interaction with molecules in AE, which can act as a reducing agent and cross-linking agent for the formation of rGO/AE hydrogel.

Additionally, we could conclude from curves c and d that the existence of AuNPs has no major impact on the FTIR spectra. The removal of the oxygen-containing functional groups located on the basal plane of GO can also be reflected from the obvious difference in interlayer spacing of GO and rGO revealed by XRD analysis.

XRD patterns of the pure GO, AE, rGO/AE, and the rGO/AE/AuNPs composite hydrogel are shown in Figure 2B. As shown in curve a, the sharp (002) peak is observed at 10.73° (d = 0.82 nm), which is attributed to the GO sample.[36] The XRD pattern of the AE shown in curve b demonstrates that AE is amorphous. The XRD patterns of the rGO/AE and rGO/AE/AuNPs composite hydrogels are present in curves c and d,
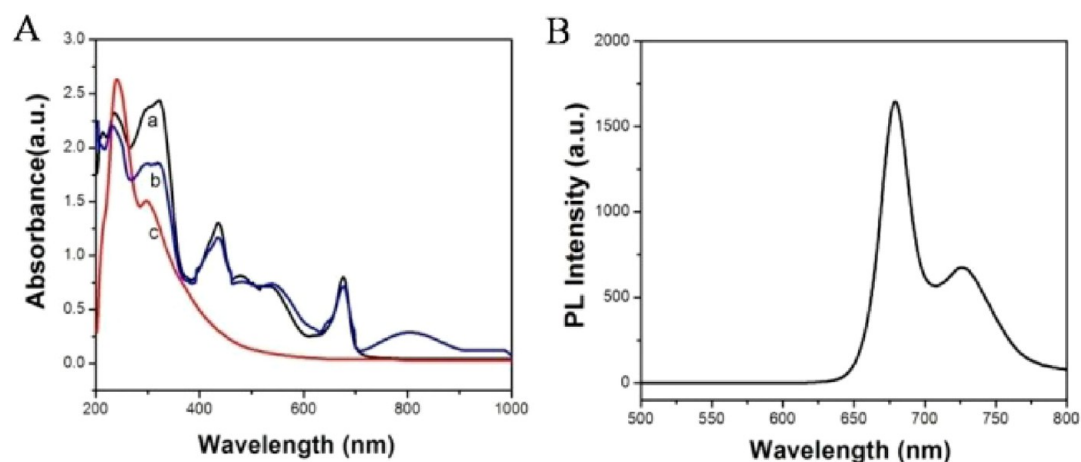
Figure 5. (A) UV−vis−NIR absorption spectra of (a) AE, (b) rGO/AE/AuNPs precursor, (c) GO; (B) Fluorescence emission spectrum of AE with 405 nm laser irradiation.
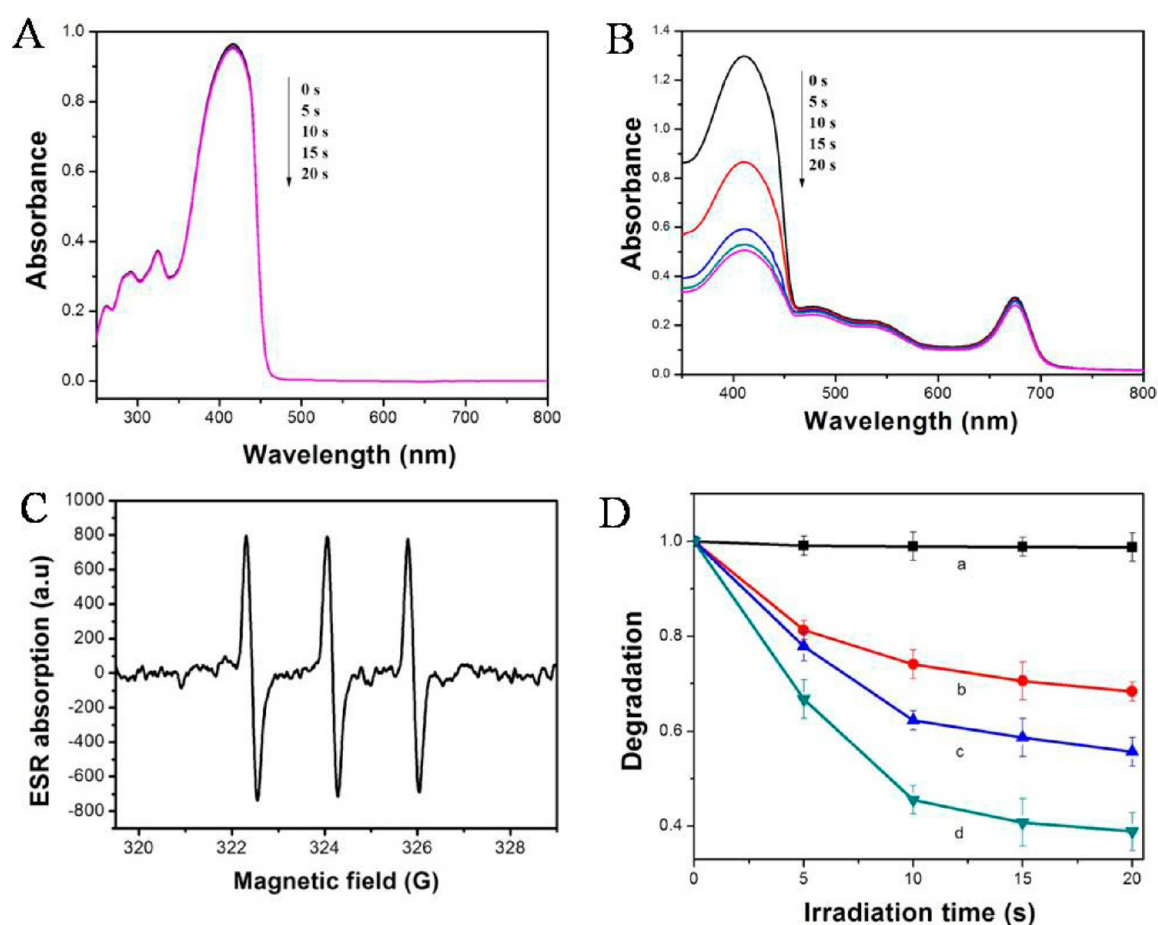

Figure 6. Photobleaching of DPBF (9.0×10^{-5} M) via the generation of $^1O_2$ in the presence of (A) nothing and (B) rGO/AE/AuNPs precursor under irradiation. (C) ESR detection of $^1O_2$ for AE, (D) time-dependent decrease in the absorbance at 410 nm via the oxidation of DPBF (9.0×10^{-5} M) with the precursor of (a) GO, (b) AE, (c) rGO/AE, and (d) rGO/AE/AuNPs under irradiation by a 660 nm laser. Error bars were based on the standard deviation of triplicate samples.

respectively. The broad diffraction peak around 27.4° ($d = 0.33$ nm) that appeared in both curves mean that GO sheets have been transformed to rGO with random packing and fewer functionalities,[37] which is caused by the reducing action of AE. And the diffraction peak at 2θ value of 38.1° is indexed to be (111) plan of AuNPs (JCPDS No. 4-0784). These results

confirm the presence of rGO and AuNPs in the composite hydrogel.

The Raman spectra of GO, rGO/AE, and rGO/AE/AuNP hydrogel are shown in Figure 2C. Two strong peaks at 1355 and 1593 cm^{-1} that are assigned to the typical D and G bands of GO are shown in curve a. The D band and G band for rGO/AE hydrogels display a small red-shift to 1352 and 1585 cm^{-1}.
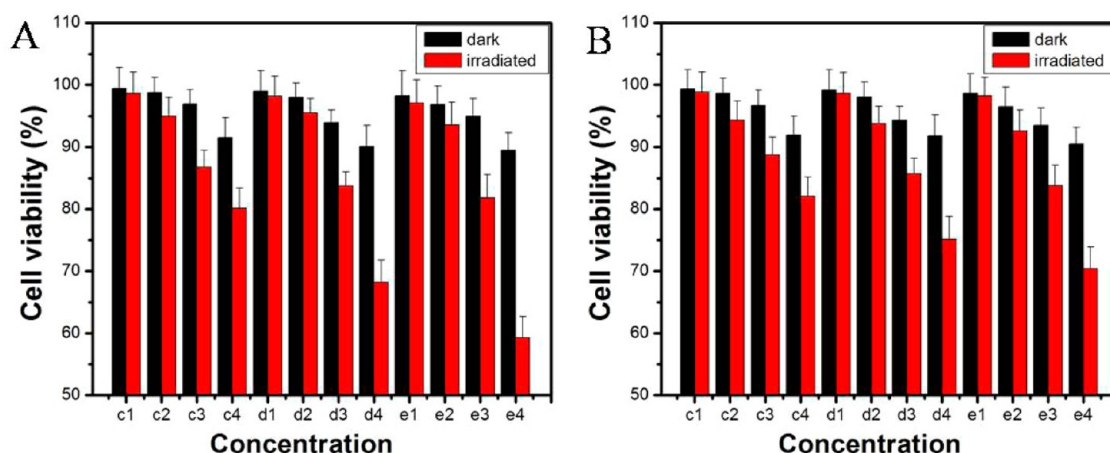
Figure 7. (A) HeLa cell and (B) CHO cell viability assay of AE (c1−c4), rGO/AE precursor (d1−d4), and rGO/AE/AuNPs precursor (e1−e4) with or without irradiation. The concentration of AE, rGO/AE, and rGO/AE/AuNPs are denoted as c, d, and e, respectively; and 1, 2, 3, and 4 are used to express the precursor diluted by DMEM with a volume factor of 1000, 100, 10 and 1, respectively.
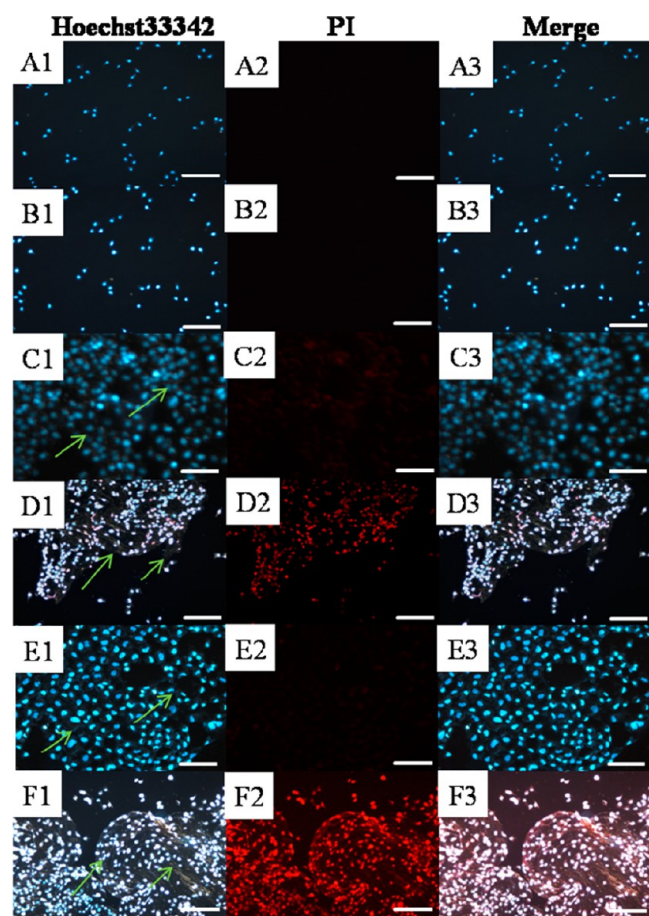

Figure 8. Fluorescence microscopy images of (A and B) bare HeLa cells, (C and D) HeLa cells incubated with rGO/AE precursor, and (E and F) the ones incubated with rGO/AE/AuNPs precursor without irradiation and after irradiation for 10 min, respectively. Each series can be classified as cell nuclei dyed blue by Hoechst 33342, cell nuclei dyed red by PI, and the merged images of both above. The scale bar is 200 μm.

And for rGO/AE/AuNPs hydrogel, the two bands shift downward to 1340 and 1580 cm^{-1}, respectively. The spectral shifts could be ascribed to the disturbance of the graphene oxide structure caused by the physical or chemical interactions

between epoxy, hydroxyl, and carboxyl moieties of GO and polar groups of AE, such as amino, carboxyl, acylamino, alkoxy, and so on. It has been acknowledged that the D band is associated with the presence of disorder in the aromatic structure or the edge effect of graphene, the G band appears due to the in-plane vibration of the sp2 carbon atoms.[38] From the spectra of the synthesized rGO/AE and rGO/AE/AuNPs hydrogels in Figure 2D, the values of I_D/I_G decrease in comparison with that of the graphite oxide. The result implies that green reduction process has caused the increase in the size of the in-plane sp2 domains and a lower level of disorder onto the graphene layer. Further characterization of rGO/AE/AuNPs hydrogel was carried out using XPS. The survey scan spectrum in Figure 2E shows that the surface of rGO/AE/AuNPs hydrogel is composed of Au, C, O and N elements. As can be seen from the inset in Figure 2E, the Au 4f$_{7/2}$ and Au 4f$_{5/2}$ peaks appear at a binding energy of 84.35 and 87.95 eV, respectively. The position of doublet peak and the peak-to-peak distance of 3.6 eV are due to metallic gold (Au^0), confirming the formation of AuNPs.[39,40] The C 1s XPS spectra of rGO/AE/AuNPs (Figure 2 F) can be fitted into four peaks centered at 285.0, 286.1, 288.4, and 290.3 eV, corresponding to C=C/C−C in aromatic rings, C−N or C−O (epoxy and alkoxy), carbonyl and carboxyl groups, respectively. The peak of C 1s is attributed to rGO sheets and AE. In Figure S4 (Supporting Information), the presence of N 1s peak at 399.55 eV indicates the existence of AE, which can be ascribed to N−C bond. And the peak of O 1s at 532.05 eV may arise from rGO and AE. These results suggest that the composite hydrogel contain rGO, AE, and AuNPs.

The morphologies, interior microstructure and elemental mapping analysis were observed by a scanning electron microscopy. Figure 3A shows a wrinkled paper like shape of GO. The images of rGO/AE hydrogel and rGO/AE/AuNPs hydrogel both present a highly porous and interconnected three-dimensional structure, as shown in Figure 3B,C, respectively. These pores arrange regularly. It is clearly seen from Figure 3D that many AuNPs are evenly distributed on the pore wall of the hydrogel throughout the 3D macroporous framework. These results suggest that many AuNPs exist in composite hydrogel and the presence of AuNPs did not significantly alter the microstructure of the hydrogel.
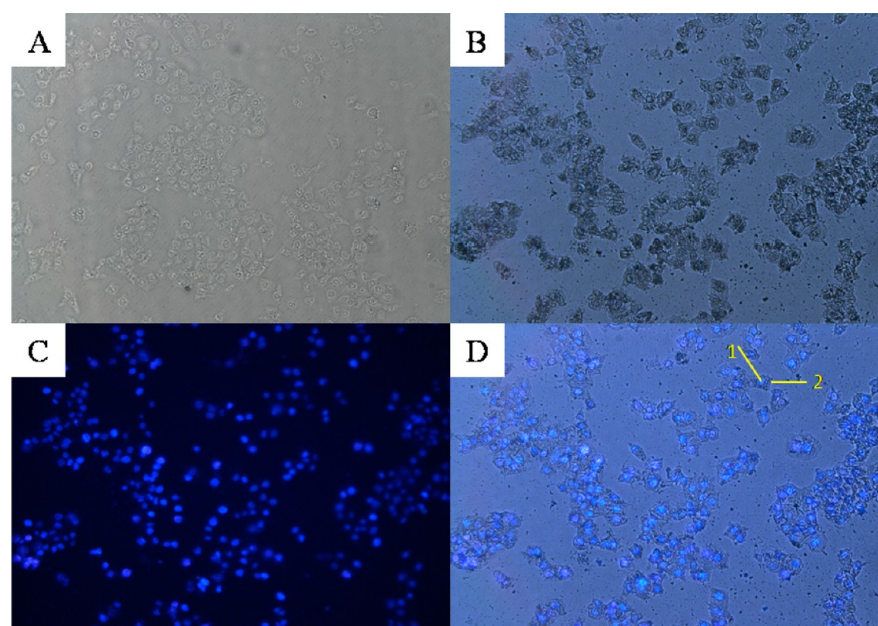
Figure 9. Optical microscope images of (A) bare HeLa cells and (B) HeLa cells coated with hydrogel shells. (C) Fluorescence microscopy image of HeLa cells with Hoechst 33342 staining coated with hydrogel shells. (D) Merged image of images B and C; straights 1 and 2 indicate HeLa cell and hydrogel shell, respectively. The scale bar is 100 μm.
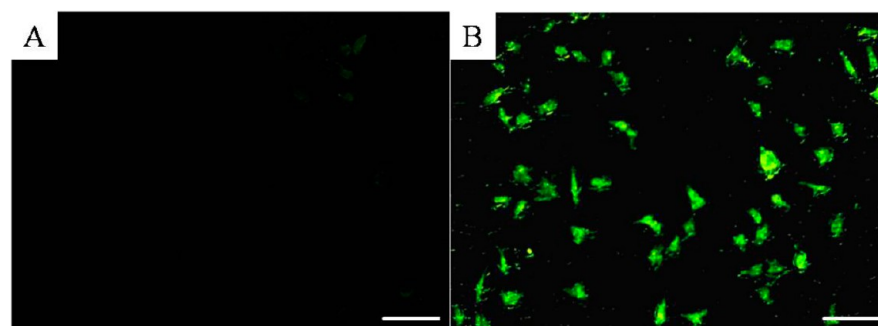

Figure 10. Fluorescence microscopy images of (A) FITC-dextran with HeLa cells and (B) FITC-dextran labeled rGO/AE/AuNPs precursor with HeLa cells. The scale bars are 50 μm.

TEM and AFM images of rGO/AE/AuNPs composite hydrogel are presented in Figure 4A,C. It can be easily observed that rGO nanosheets have irregular shape and are decorated with many AuNPs. These particles are not homogeneous. One possible explanation may be that AE-mediated formation of AuNPs growth occurs through the adventitious interaction of shape-directing molecules presented in AE and the distribution of these functional groups is random, such as carbonyl groups, aldehydic or ketonic carbons, aromatic carbons of biomolecules, and hydroxyl groups.[9] Figure 4D shows cross-sectional analysis of AuNPs attached onto the surface of rGO sheets. The average size of AuNPs is about 35 nm (Figure 4A,D), very few AuNPs reside outside the rGO support. The formation of nanocomposite is due to an electrostatic attraction between negatively charged rGO sheets and positively charged AuNPs. The contact angle of rGO/AE/AuNPs hydrogel film was measured to check its hydrophilicity. As shown in Figure 4B, the static contact angle is only 13.6°, indicating a good hydrophilicity of the hydrogel film. The as-prepared AuNPs have a surface plasmon resonance wavelength of 800 nm, as shown in the UV−vis−NIR absorption spectrum (Figure 4E), which means that the AuNPs have the ability to absorb NIR light. To further prove the potential use of rGO/AE/AuNPs as a PTT agent, we also observed and measured a time-dependent photothermal effect under irradiation by an 808 nm NIR laser at a power density of 200 mW·cm^{-2}. Figure 4F shows the IR thermal images of AuNPs, GO, rGO/AE, and rGO/AE/AuNPs when exposed to the laser for 10 min, and the average temperatures of the samples increase from 34.0 to 36.5, 35.7, 38.9, and 40.1 °C, respectively. The curves in Figure 4G show a rapid temperature increase during the first 10 min and a slow temperature variation from 10 to 15 min. Moreover, the highest temperature increase of rGO/AE/AuNPs solution is up to 6.3 °C within 15 min, whereas the water temperature increases by only 0.9 °C under the same laser exposure. These results further confirm that AuNPs and rGO both have good photothermal effect, and the combination of rGO/AE/AuNPs could serve as a synergistic platform for efficient hyperthermia therapy.

As shown in Figure 5A, AE exhibits two UV-absorbing bands in 225−260 nm and 265−365 nm associated with vitamin C and polypeptide amino acid respectively,[35] as well as two characteristic absorbance bands in the vis−NIR regions (curve a): a bluish violet-absorbing band in 390−460 nm and a red-

absorbing band in 630−690 nm, which correspond to the absorption range of chlorophyll.[7] Due to its obvious absorption in 630−690 nm, AE is able to be excited by using 660 nm light and could be used as a photosensitizer. The UV−vis spectrum of GO is presented in Figure 4A (c); its characteristic absorption bands at 233 and 305 nm corresponds to $\pi \rightarrow \pi^*$ (C=C) and n $\rightarrow$ p*(C=O) transition, respectively. In the UV−vis−NIR absorption spectrum of rGO/AE/AuNPs precursor (curve b), we observe not only the characteristic bands of both AE and rGO, but also the broad peak at about 800 nm assigned to AuNPs. These results confirm the presence of the rGO, AuNPs, and AE in the composite hydrogel. The fluorescence emission spectrum of AE in ethanol is shown in Figure 5B. With the excitation wavelength of 405 nm, the emission maximum of photoluminescence spectrum of AE is around 680 nm, which is consistent with the photoluminescence spectrum of chlorophyll,[7] suggesting that chlorophyll derivatives exist in AE.

Singlet oxygen generation is the critical step in PDT, thus we investigated the $^1O_2$ generation abilities of the precursors. No obvious change in the maximum absorption of DPBF at 410 nm could be observed under irradiation in the presence of nothing or pure GO (Figure 6A and curve A in Figure S2, Supporting Information). Whereas, the decrease in the absorbance of DPBF is clear after irradiation for 20 s when AE or rGO/AE/AuNPs hydrogel exists (Figure 6B and curves B, C, D in Figure S2, Supporting Information). The result suggests that pure GO does not produce singlet oxygen under light illumination, but AE play a major role in the whole photobleaching experiment of DPBF. To confirm the results of DPBF experiments, we used ESR spin trapping spectroscopy to detect $^1O_2$ generated via the NIR irradiation of AE at 660 nm. $^1O_2$ can oxidize TEMP into stable N-oxyl radical TEMPO, whose paramagnetic ESR spectrum shows a symmetrical triplet hyperfine lines.[41] The ESR signal of TEMPO in Figure 6C and $^1O_2$ production during photochemical reaction of the AE with oxygen confirm that AE can be used in PDT. Furthermore, Figure 6D shows that the DPBF with rGO/AE/AuNPs exhibits faster degradation than with AE, rGO/AE under irradiation. An explanation for the result may be that, as an excellent electron acceptor, rGO can decrease the recombination rate of the electron−hole pairs and increase the quantum efficiency of the photosensitization process, thus enhancing the generation of ROS. These results indicate that AuNPs and rGO have a synergistic effect on accelerating the generation of $^1O_2$. Therefore, the rate of singlet oxygen production may be controlled by adjusting the content of AE to achieve a better antitumor effect.

Although the UV−vis−NIR adsorption of rGO/AE/AuNPs precursor decline gradually with the increase of irradiated time (Figure S3, Supporting Information), the spectrum irradiated for 80 min still has a moderate absorbance peak at 630−690 nm, which indicates that the rGO/AE/AuNPs hydrogel could be used in intermittent PDT.

Cell Viability. The relative viabilities of HeLa cells (cancerous cells) and CHO cells (normal cells without expression of epidermal growth factor receptor) cultured with all the precursors were examined via the standard MTT assay and are shown in Figure 7. As expected, all the cell survival rates show a downward trend as the concentration of precursor increases. However, even when the solution of AE, rGO/AE, and rGO/AE/AuNPs precursor was not diluted with DMEM (denoted c4, d4 and e4), the relative cell survival rates in the

dark are still 91.5, 90.1, and 89.5%, respectively. A similar dose-dependent cytotoxicity behavior was observed on CHO cells, but to a lower extent. The results indicate that all the samples are biocompatible and have low cytotoxicities on both kinds of cells. However, after 10 min of sequential NIR irradiation, the relative viabilities of HeLa cells treated by AE, rGO/AE, and rGO/AE/AuNPs precursor (without dilution by culture medium) sharply decrease to 80.1, 68.2, and 59.3%. Moreover, rGO/AE/AuNPs precursor showed remarkably higher anti-cancer efficiency than rGO/AE and AE precursor at each concentration. The results reveal that the presence of AuNPs or rGO in the precursors can accelerate cell death, and the rGO/AE/AuNPs hydrogel can serve as a potential high-performance platform for synergistic antitumor effects. As for CHO cells, the relatively low killing efficiency and inconspicuous dose-dependent cytotoxicity can be attributed to the minimal internalization of the precursors, owing to a lack of epidermal growth factor receptor on the CHO cell surface.[42]

Fluorescence Images. The antitumor effects of the rGO/AE and rGO/AE/AuNPs precursors were further investigated by fluorescence microscope with PI/Hoechst 33342 double staining. Hoechst 33342 can freely pass through cell membranes and stain nuclear DNA blue, while PI is only able to enter necrotic cells or late-phase apoptotic cells to stain nuclear DNA red.[43] Fluorescence images of HeLa cells under different conditions are shown in Figure 8. As a control group (Figure 8A,B), bare HeLa cells grow exuberantly before or even after laser irradiation, without their nuclei appearing red. Figure 8C,E shows cells incubated with rGO/AE and rGO/AE/AuNPs precursor without NIR irradiation, respectively. No significant cell damage was noticed as only faint red fluorescence signals could be seen, which indicates the good biocompatibility and low toxicity of rGO/AE/AuNPs precursor. When subjected to NIR irradiation for 10 min, strong red fluorescence image and purple merged image in Figure 8D,F can be observed. This demonstrates that HeLa cells are effectively killed by the $^1O_2$ and local hyperthermia, which is in agreement with the MTT results. HeLa cells treated by rGO/AE/AuNPs were effectively killed after laser exposure, while rGO/AE treated cells were less destroyed, which collectively demonstrates that functionalized rGO/AE/AuNPs composite could serve as a potential PTT/PDT platform for multiple antitumor therapy. Besides, a hydrogel shell on HeLa cells in Figure 8C−F (green arrows) could also be seen.

The formation of the hydrogel on the surface of cells in situ was further investigated. The optical microscopic images of the HeLa cells without and with rGO/AE/AuNPs coated are presented in Figure 9A,B. From comparison of both images, it is easily observed that the surface of HeLa cells in Figure 9B is covered with a thin and semitransparent shell. Figure 9C presents fluorescence microscopy image of HeLa cells coated with hydrogel shells with Hoechst 33342 staining, and Figure 9D is the merged image of B and C. As shown in Figure 9D, a thin and obvious hydrogel shell (indicated by straight 2) on the cells (straight 1) can be seen. The results indicate that the hydrogel shell can be successfully formed on the HeLa cells in situ. It contributes to retaining a high drug concentration on the tumor cells and prevents them from migrating to normal tissue, thus reducing the side effects.

Cellular Uptake. The cellular uptake of FITC-dextran and precursor labeled by FITC-dextran were observed via fluorescence microscopy with a 488 nm excitation wavelength. As shown in Figure 10A, there is almost no fluorescence within

the cells. In contrast, intense green fluorescence is clearly visible in the entire cell from Figure 10B, which implies that precursor with FITC-dextran labeling were successfully internalized into the cell interior. A possible explanation for this result could be that CD44 receptors protein[44] on HeLa cells is responsible for the efficient cellular uptake of rGO/AE/AuNPs precursor labeled by FITC-dextran, which was converted into the composite hydrogel under NIR irradiation and prevented FITC-dextran emigrating from the labeled cell. It is believed that the contact of CD44 receptors with the precursor is dominated by hydrogen bonds and van der Waals forces between carboxyl groups and N-acetyl groups in rGO/AE/AuNPs precursor and receptors protein on the cell membrane.[34] For the same reason, the hydrogel shell on the tumor cell could also retain a high concentration of PS and photothermal agents on lesions and prevent their migration to normal tissue, thereby enhancing the curative effect.

CONCLUSION

We have demonstrated that the multisynergistic rGO/AE/AuNPs composite hydrogel could serve as PDT/PTT integrated platform for enhanced cancer therapy by utilizing sequential irradiation as stimuli. The AuNPs homodispersed in the hydrogel and rGO both exhibit a conspicuous photothermal effect for increasing the local temperature under NIR laser irradiation. The combination of AuNPs and rGO also effectively improves $^1O_2$ generation. AE performs multiple roles in the formation of hydrogel and killing tumor cells under NIR irradiation, such as a cross-linking agent, reductant, and photosensitizer and tricomponent composite hydrogel not only displays cooperative antitumor properties but also affords the system good biocompatibility and dispersibility in water and physiological environment. This system has remarkable photo-dynamic sensitization and photothermy under laser irradiation along with the entry of AE into cells, also could be used for loading other medicines such as chemotherapeutics. This approach, the combination of PTT/PDT and localized gelation via the mode of photoregulation, demonstrates a synergistic effect on the destruction of cancer cells and holds promise for future applications in multiple antitumor therapies.

ASSOCIATED CONTENT

Ⓢ Supporting Information
Zeta potentials, UV−vis detection of DPBF decomposition correlated to the absorbance decay at 410 nm, UV−vis−NIR absorption spectra of rGO/AE/AuNPs precursor and XPS spectra of the O 1s region, N 1s region of rGO/AE/AuNPs hydrogels. The Supporting Information is available free of charge on the ACS Publications website at DOI: 10.1021/acsami.5b03907.

AUTHOR INFORMATION

Corresponding Authors
*E-mail: s_yuhua@163.com.
*E-mail: anjx@163.com.
Notes
The authors declare no competing financial interest.

ACKNOWLEDGMENTS

REFERENCES

(1) Yang, K.; Wan, J.; Zhang, S.; Tian, B.; Zhang, Y. J.; Liu, Z. The Influence of Surface Chemistry and Size of Nanoscale Graphene Oxide on Photothermal Therapy of Cancer using Ultra-low Laser Power. *Biomaterials* **2012**, *33*, 2206−2214.

(2) Zhou, Z. G.; Kong, B.; Yu, C.; Shi, X. Y.; Wang, M. W.; Liu, W.; Sun, Y. N.; Zhang, Y. J.; Yang, H.; Yang, S. P. Tungsten Oxide Nanorods: An Efficient Nanoplatform for Tumor CT Imaging and Photothermal Therapy. *Sci. Rep.* **2014**, *4*, 3653−3662.

(3) Yong, Y.; Zhou, L. J.; Gu, Z. J.; Yan, L.; Tian, G.; Zheng, X. P.; Liu, X. D.; Zhang, X.; Shi, J. X.; Cong, W. S.; Yin, W. Y.; Zhao, Y. L. WS$_2$ Nanosheet as a New Photosensitizer Carrier for Combined Photodynamic and Photothermal Therapy of Cancer Cells. *Nanoscale* **2014**, *6*, 10394−10403.

(4) Hu, Z.; Li, J.; Li, C.; Zhao, S.; Li, N.; Wang, Y.; Wei, F.; Chen, L.; Huang, Y. D. Folic Acid-Conjugated Grapheme-ZnO Nanohybrid for Targeting Photodynamic Therapy under Visible Light Irradiation. *J. Mater. Chem. B* **2013**, *1*, 5003−5013.

(5) Asadirad, A. M.; Erno, Z.; Branda, N. R. Photothermal Release of Singlet Oxygen from Gold Nanoparticles. *Chem. Commun.* **2013**, *49*, 5639−5641.

(6) Zhang, Y.; Qian, J.; Wang, D.; Wang, Y.; He, S. Multifunctional Gold Nanorods with Ultrahigh Stability and Tunability for in Vivo Fluorescence Imaging, SERS Detection, and Photodynamic Therapy. *Angew. Chem., Int. Ed.* **2013**, *52*, 1148−1151.

(7) Yang, X.; Xiao, Q.; Niu, C.; Jin, N.; Ouyang, J.; Xiao, X.; He, D. Multifunctional Core−Shell Upconversion Nanoparticles for Targeted Tumor Cells Induced by Near-Infrared Light. *J. Mater. Chem. B* **2013**, *1*, 2757−2763.

(8) Ulatowska-Jarza, A.; Zychowicz, J.; Holowacz, I.; Bauer, J.; Razik, J.; Wieliczko, A.; Podbielska, H. E.; Müller, G.; Stręk, W.; Bindig, U. Antimicrobial PDT with Chlorophyll-derived Photosensitizer and Semiconductor Laser. *Med. Laser Appl.* **2006**, *21*, 177−183.

(9) Shankar, S. S.; Rai, A.; Ahmad, A.; Sastry, M. Controlling the Optical Properties of Lemongrass Extract Synthesized Gold Nano-triangles and Potential Application in Infrared-Absorbing Optical Coatings. *Chem. Mater.* **2005**, *17*, 566−572.

(10) Li, W. T.; Tsao, H. W.; Chen, Y. Y.; Cheng, S. W.; Hsu, Y. C. A Study on the Photodynamic Roperties of Chlorophyll Derivatives using Human Hepatocellular Carcinoma Cells. *Photochem. Photobiol. Sci.* **2007**, *6*, 1341−1348.

(11) Yoshii, H.; Yoshii, Y.; Asai, T.; Furukawa, T.; Takaichi, S.; Fujibayashi, Y. Photo-Excitation of Carotenoids Causes Cytotoxicity via Singlet Oxygen Production. *Biochem. Biophys. Res. Commun.* **2012**, *417*, 640−645.

(12) Skalkos, D.; Gioti, E.; Stalikas, C. D.; Meyer, H.; Papazoglou, T. G.; Filippidis, G. Photophysical Properties of Hypericum *Perforatum* L. Extracts—Novel Photosensitizers for PDT. *J. Photochem. Photobiol., B* **2006**, *82*, 146−151.

(13) Zhou, L.; Jiang, H.; Wei, S.; Ge, X.; Zhou, J.; Shen, J. High-Efficiency Loading of Hypocrellin B on Graphene Oxide for Photodynamic Therapy. *Carbon* **2012**, *50*, 5594−5604.

(14) Bergquist, S. A. M.; Gertsson, U. E.; Olsson, M. E. Influence of Growth Stage and Postharvest Storage on Ascorbic acid and Carotenoid Content and Visual Quality of Baby Spinach (*Spinacia oleracea* L.). *J. Sci. Food Agric.* **2006**, *86*, 346−355.

(15) Adhikari, B.; Biswas, A.; Banerjee, A. Graphene Oxide-Based Hydrogels to Make Metal Nanoparticle-Containing Reduced Graphene Oxide-Based Functional Hybrid Hydrogels. *ACS Appl. Mater. Interfaces* **2012**, *4*, 5472−5482.

(16) Adhikari, B.; Biswas, A.; Banerjee, A. Graphene Oxide-Based Supramolecular Hydrogels for Making Nanohybrid Systems with Au Nanoparticles. *Langmuir* **2012**, *28*, 1460−1469.

(17) Adhikari, B.; Banerjee, A. Short Peptide Based Hydrogels: Incorporation of Graphene into the Hydrogel. *Soft Matter* **2011**, *7*, 9259−9266.

(18) Cong, H. P.; Ren, X. C.; Wang, B.; Yu, S. H. Macroscopic Multifunctional Graphene-based Hydrogels and Aerogels by a Metal Ion Induced Self-Assembly Process. *ACS Nano* **2012**, *6*, 2693−2703.

(19) Li, D.; Mueller, M. B.; Gilje, S.; Kaner, R. B.; Wallace, G. G. Processable Aqueous Dispersions of Graphene Nanosheet. *Nat. Nanotechnol.* **2008**, *3*, 101−105.

(20) Hu, S. H.; Chen, Y. W.; Hung, W. T.; Chen, I. W.; Chen, S. Y. Quantum-Dot-Tagged Reduced Graphene Oxide Nanocomposites for Bright Fluorescence Bioimaging and Photothermal Therapy Monitored in situ. *Adv. Mater.* **2012**, *24*, 1748−1754.

(21) Robinson, J. T.; Tabakman, S. M.; Liang, Y.; Wang, H.; Casalongue, H. S.; Vinh, D.; Dai, H. Ultrasmall Reduced Graphene Oxide with High Near-Infrared Absorbance for Photothermal Therapy. *J. Am. Chem. Soc.* **2011**, *133*, 6825−6831.

(22) Yang, K.; Zhang, S.; Zhang, G. .; Sun, X. M.; Lee, S. T.; Liu, Z. Graphene in Mice: Ultrahigh in Vivo Tumor Uptake and Efficient Photothermal Therapy. *Nano Lett.* **2010**, *10*, 3318−3323.

(23) Tian, B.; Wang, C.; Zhang, S.; Feng, L. Z.; Liu, Z. Photothermally Enhanced Photodynamic Therapy Delivered by Nano-graphene Oxide. *ACS Nano* **2011**, *S*, 7000−7009.

(24) Gao, L.; Fei, J.; Zhao, J.; Li, H.; Cui, Y.; Li, J. Hypocrellin-Loaded Gold Nanocages with High Two-Photon Efficiency for Photothermal/Photodynamic Cancer Therapy in Vitro. *ACS Nano* **2012**, *6*, 8030−8040.

(25) Kuo, W. S.; Chang, C. N.; Chang, Y. T.; Yang, M. H.; Chien, Y. H.; Chen, S. J.; Yeh, C. S. Gold Nanorods in Photodynamic Therapy, as Hyperthermia Agents, and in Near-Infrared Optical Imaging. *Angew. Chem.* **2010**, *122*, 2771−2775.

(26) Wang, J.; Zhu, G.; You, M.; Song, E.; Shukoor, M. I.; Zhang, K.; Altman, M. B.; Chen, Y.; Zhu, Z.; Huang, C. Z.; Tan, W. Assembly of Aptamer Switch Probes and Photosensitizer on Gold Nanorods for Targeted Photothermal and Photodynamic Cancer Therapy. *ACS Nano* **2012**, *6*, 5070−5077.

(27) Li, F.; Park, S. J.; Ling, D.; Park, W.; Han, J. Y.; Na, K.; Char, K. Hyaluronic Acid-Conjugated Graphene Oxide/Photosensitizer Nanohybrids for Cancer Targeted Photodynamic Therapy. *J. Mater. Chem. B* **2013**, *1*, 1678−1686.

(28) Chen, Z. W.; Li, Z. H.; Wang, J. S.; Ju, E. G.; Zhou, L.; Ren, J. S.; Qu, X. G. A Multi-synergistic Platform for Sequential Irradiation-Activated High-Performance Apoptotic Cancer Therapy. *Adv. Funct. Mater.* **2014**, *24*, 522−529.

(29) Hummers, W. S.; Offeman, R. E. Preparation of Graphitic Oxide. *J. Am. Chem. Soc.* **1958**, *80*, 1339−1339.

(30) Awuah, S. G.; Polreis, J.; Biradar, V.; You, Y. Singlet Oxygen Generation by Novel NIR BODIPY Dyes. *Org. Lett.* **2011**, *13*, 3884−3887.

(31) Kundu, B.; Kundu, S. C. Silk Sericin/Polyacrylamide in Situ Forming hydrogels for Dermal Reconstruction. *Biomaterials* **2012**, *33*, 7456−7467.

(32) Takayama, K.; Hirose, H.; Tanaka, G.; Pujals, S.; Katayama, S.; Nakase, I.; Futaki, S. Effect of the Attachment of a Penetration Accelerating Sequence and the Influence of Hydrophobicity on Octaarginine-Mediated Intracellular delivery. *Mol. Pharmaceutics* **2012**, *9*, 1222−1330.

(33) Sui, Z. Y.; Zhang, X. T.; Lei, Y.; Luo, Y. J. Easy and Green Synthesis of Reduced Graphite Oxide-based Hydrogels. *Carbon* **2013**, *49*, 4314−4321.

(34) Wu, H. X.; Shi, H. L.; Wang, Y. P.; Jia, X. Q.; Tang, C. Z.; Zhang, J. M.; Yang, S. P. Hyaluronic Acid Conjugated Graphene Oxide for Targeted Drug Delivery. *Carbon* **2014**, *69*, 379−389.

(35) Bouropoulos, N.; Weiner, S.; Addadi, L. Calcium Oxalate Crystals in Tomato and Tobacco Plants: Morphology and in vitro Interactions of Crystal-Associated Macromolecules. *Chem.—Eur. J.* **2001**, *7*, 1881−1888.

(36) Krishnamoorthy, K.; Veerapandian, M.; Yun, K.; Kim, S. J. The Chemical and Structural Analysis of Graphene Oxide with Different Degrees of Oxidation. *Carbon* **2013**, *53*, 38−49.

(37) Zhang, Y.; Zhang, N.; Tang, Z. R.; Xu, Y. J. Graphene Transforms Wide Band Gap ZnS to a Visible Light Photocatalyst. The New Role of Graphene as a Macromolecular Photosensitizer. *ACS Nano* **2012**, *6*, 9777−9789.

(38) Singh, V.; Joung, D.; Zhai, L.; Das, S.; Khondaker, S. I.; Seal, S. Graphene Based Materials: Past, Present and Future. *Prog. Mater. Sci.* **2011**, *56*, 1178−1271.

(39) Yin, H. J.; Tang, H. J.; Wang, D.; Gao, Y.; Tang, Z. Y. Facile Synthesis of Surfactant-free Au Cluster/Graphene Hybrids for High-Performance Oxygen Reduction Reaction. *ACS Nano* **2012**, *6*, 8288−8297.

(40) Turner, M.; Golovko, V. B.; Vaughan, O. P. H.; Abdulkin, P.; Murcia, A. B.; Tikhov, M. S.; Johnson, B. F. G.; Lambert, R. M. Selective Oxidation with Dioxygen by Gold Nanoparticle Catalysts Derived from 55-Atom Clusters. *Nature* **2008**, *454*, 981−983.

(41) Lion, Y.; Delmelle, M.; Vorst, V. D. New Method of Detecting Singlet Oxygen Production. *Nature* **1976**, *263*, 442−443.

(42) Ahsan, A.; Hiniker, S. M.; Davis, M. A.; Lawrence, T. S.; Nyati, M. K. Role of Cell Cycle in Epidermal Growth Factor Receptor Inhibitor-Mediated Radiosensitization. *Cancer Res.* **2009**, *69*, 5108−5114.

(43) Zhao, J.; Huang, Y.; Song, Y.; Zhao, X.; Jin, J.; Wang, J.; Huang, L. Low Osmolar Contrast Medium Induces Cellular Injury and Disruption of Calcium Homeostasis in Rat Glomerular Endothelial Cells in Vitro. *Toxicol. Lett.* **2009**, *185*, 124−131.

(44) Ma, M.; Chen, H. R.; Chen, Y.; Zhang, K.; Wang, X.; Cui, X. Z.; Shi, J. L. Hyaluronic Acid-Conjugated Mesoporous Silica Nanoparticles: Excellent Colloidal Dispersity in Physiological Fluids and Targeting Efficacy. *J. Mater. Chem.* **2012**, *22*, 5615−5621.